

PAPER

Doppler Velocity Decomposition Based Radar Imaging by 79 GHz Band Millimeter Wave Radar

Yoshiki SEKIGAWA[†], *Nonmember and* Shouhei KIDERA^{†a)}, *Senior Member*

SUMMARY The Doppler velocity enhanced 79 GHz band millimeter wave (MMW) radar imaging approach is presented here, assuming a human body imaging or recognition application. There are numerous situations in which the spatial resolution is insufficient, due to aperture angle limitations, especially for vehicle mounted MMW radar systems. As the 79 GHz band MMW radar has a definitive advantage for higher Doppler velocity resolution even with a short coherent processing interval (CPI), this study introduces the Doppler velocity decomposed imaging scheme, focusing on micro-Doppler variations of the walking human model. The real experimental data show that our proposed approach provides further improvement for accurate and high resolution radar imaging.

key words: millimeter wave (MMW) radar, micro-Doppler velocity decomposition, 79 GHz band, human body imaging

1. Introduction

High-frequency millimeter wave (MMW) radar is the most emergent sensing technique, having numerous advantages in terms of high spatial resolution and compact modules, and is also promising for various sensing applications, such as collision avoidance for self-driving or advance driver assistant systems (ADAS), which are applicable even in optically invisible situations (e.g., dense smog or bad weather). However, there are still challenging issues in MMW radar imaging: its spatial resolution is severely limited by the aperture size, which cannot be expanded in vehicle-mounted radar systems. In far-range sensing cases, such as more than 10 m, the aperture angle also becomes critically small, and a necessary spatial resolution for object recognition is hardly available.

There are many radar imaging schemes that assume the MMW MIMO observation model [1], and they are mostly based on coherent integration (CI) schemes, such as Kirchhoff migration [2], the range migration algorithm (RMA) [3]–[6], diffraction tomography [7], [8], and sparse regularization schemes [9]–[11]. Nonetheless, the above approaches inherently suffer from a limited spatial resolution. To overcome the above challenging issues, this study focuses on the Doppler velocity decomposed CI imaging approach, because the higher MMW band, such as the 79 GHz band, provides a much higher Doppler velocity resolution, even when assuming a short coherent processing interval

(CPI). Specifically, sufficiently high temporal and velocity resolutions are available in this frequency band. Assuming the scenario that a target consists of multiple parts of objects with different velocities, such as walking human motion, each Doppler velocity spectrum is separated and processed for post CI imaging. The above approach is predicted to be effective, especially for human body imaging, because its left and right arms or legs have considerably large variations in walking motions, whose Doppler velocity is easily separated by the MMW radar specification with high temporal resolution.

To the best of our knowledge, there are few studies on Doppler enhanced radar imaging schemes [12], [13], while a number of studies have focused on improving an equivalent range resolutions using Doppler spectra decomposition [14]. The study [12] introduced motion based separation for closely located object, however, it requires the inverse synthetic aperture process to enhance the spatial resolution with a motion parameter pre-estimation. While our previous study [13] introduced the Doppler decomposed RMA scheme, it validates only the numerical data and assumes the lower MMW band, such as 10 GHz or 20 GHz. Notably, numerous studies have been conducted on the range-Doppler algorithm for synthetic aperture radar (SAR) and inverse SAR (ISAR) scenario [15], [16]. These studies highlighted the need to compensate for the Doppler frequency variance to maintain angular resolution. However, the algorithm does not provide a method to decompose the responses from multiple targets within the same angular resolution when these targets exhibit different Doppler velocities. In addition, the wavenumber and Doppler velocity decomposition scheme for the different radar imaging scheme known as range points migration (RPM) has been introduced to improve the reconstruction accuracy [17]. However, RPM relies on incoherent conversion from the measured time-of-flight (TOF) points to their associated reflection points, and may not offer sufficient accuracy, particularly for the actual human model, due to limitation of an aperture size or range (TOF) resolution. In contrast, this study investigates a real walking human model with 79 GHz MIMO radar, where higher resolutions in both velocity and temporal axis provide more reliable reconstruction performances. Note that, the part of which has been demonstrated in [18], it only introduces the simple metallic spheres targets. In addition, the weighted CI schemes are incorporated into this scheme to suppress a side-lobe effect. These experimental results, carried out in an anechoic chamber, demonstrate that our

Manuscript received November 7, 2023.

Manuscript revised February 19, 2024.

Manuscript publicized July 18, 2024.

[†]Graduate School of Informatics and Engineering, The University of Electro-Communications, Chofu-shi, 182-8585 Japan.

a) E-mail: kidera@uec.ac.jp

DOI: 10.23919/transcom.2023EBP3175

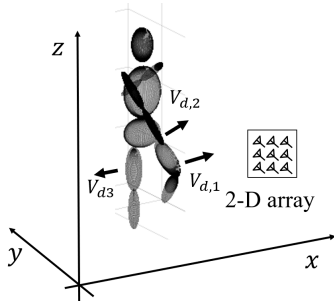


Fig. 1 Observation model.

proposed scheme effectively decomposes each part of the human body associated with Doppler velocity.

2. Method

2.1 Observation Model

Figure 1 shows the observation model. Either pulse Doppler radar or frequency modulated continuous wave (FMCW) radar is applicable in this model, if a complex-valued range profile is available in each pulse hit. A number of transmitters and receivers are configured on the $y = 0$ plane, the locations of which are defined as $\mathbf{r}_T = (X_T, 0, Z_T)$ and $\mathbf{r}_R = (X_R, 0, Z_R)$, respectively. The scattered response as $\tilde{s}(t, \tau, \mathbf{r}_T, \mathbf{r}_R)$ is defined, where t and τ denote the fast and slow times, respectively.

2.2 Doppler Decomposed CI Method

The Doppler velocity based CI approach is presented as follows. Assuming that multiple objects take different motions, multiple Doppler spectra belonging to each part of the object are clearly separated. Thus, the clustering process in terms of Doppler velocity would be effective for generating Doppler separated or associated CI images, which apparently enhances the spatial resolution of the traditional CI images.

First, the scattered data $\tilde{s}(t, \tau, \mathbf{r}_T, \mathbf{r}_R)$ are converted to range-Doppler data using the 1-D Fourier transform along the slow time τ as:

$$s(t, v_d, \mathbf{r}_T, \mathbf{r}_R) = \int_T \tilde{s}(t, \tau, \mathbf{r}_T, \mathbf{r}_R) \exp\left\{-j\frac{4\pi v_d}{\lambda}\tau\right\} d\tau \quad (1)$$

where λ is the center wavelength, and T is the so-called CPI, which determines the temporal resolution. Then, the local peaks of $s(t, v_d, \mathbf{r}_T, \mathbf{r}_R)$, defined as $(\tilde{t}_i, \tilde{v}_{d,i})$ ($i = 1, \dots, N_{v_d}$), where N_{v_d} denotes the number of local peaks are extracted as:

$$\left. \begin{aligned} \frac{\partial |s(t, v_d, \mathbf{r}_T, \mathbf{r}_R)|}{\partial v_d} &= 0 \\ \frac{\partial |s(t, v_d, \mathbf{r}_T, \mathbf{r}_R)|}{\partial t} &= 0 \\ |s(t, v_d, \mathbf{r}_T, \mathbf{r}_R)| &\geq \alpha \max_{(t, v_d)} |s(t, v_d, \mathbf{r}_T, \mathbf{r}_R)| \end{aligned} \right\}. \quad (2)$$

where α is the threshold parameter and holds $0 \leq \alpha \leq 1$.

The parameter α is If the Doppler spectrum of each part is separated, the following filtering in (t, v_d) space for each $(\tilde{t}_i, \tilde{v}_{d,i})$ is applied as:

$$\begin{aligned} \bar{s}(t, \tau, \mathbf{r}_T, \mathbf{r}_R; \tilde{t}_i, \tilde{v}_{d,i}) &= \frac{1}{2\pi} \int W(t, v_d; \tilde{t}_i, \tilde{v}_{d,i}) \\ &\times s(t, v_d, \mathbf{r}_T, \mathbf{r}_R) \exp\left(-j\frac{4\pi v_d}{\lambda}\tau\right) dv_d \end{aligned} \quad (3)$$

where $W(t, v_d; \tilde{t}_i, \tilde{v}_{d,i})$ denotes the windowing function with the center of $(\tilde{t}_i, \tilde{v}_{d,i})$ in (t, v_d) space. Notably, the window width of $W(t, v_d; \tilde{t}_i, \tilde{v}_{d,i})$ should be set to the available Doppler velocity resolution obtained using the assumed CPI and wavelength to attain a reflection response with same Doppler velocity in the v_d space. This will enable it to suppress the interfering effect from responses with different Doppler velocities.

Finally, the CI process is applied to each decomposed signal $\bar{s}(t, \tau, \mathbf{r}_T, \mathbf{r}_R; \tilde{t}_i, \tilde{v}_{d,i})$ to provide the Doppler associated radar image as $I(\mathbf{r}, \tau; \tilde{v}_{d,i})$ using the following equation as:

$$\begin{aligned} I(\mathbf{r}, \tau; \tilde{v}_{d,i}) &= \sum_{\mathbf{r}_T, \mathbf{r}_R} w(\mathbf{r}_T, \mathbf{r}_R) \int_{-\infty}^{\infty} \bar{S}(\omega, \tau, \mathbf{r}_T, \mathbf{r}_R; \tilde{t}_i, \tilde{v}_{d,i}) \\ &\times G_R^*(\omega, \mathbf{r}, \mathbf{r}_R) G_T^*(\omega; \mathbf{r}_T, \mathbf{r}) d\omega \end{aligned} \quad (4)$$

where $*$ denotes the complex conjugate, $\bar{S}(\omega, \tau, \mathbf{r}_T, \mathbf{r}_R; \tilde{t}_i, \tilde{v}_{d,i})$ denotes the 1-D Fourier transform of $\bar{s}(t, \tau, \mathbf{r}_T, \mathbf{r}_R; \tilde{t}_i, \tilde{v}_{d,i})$ in terms of t . $G_T(\omega; \mathbf{r}_T, \mathbf{r})$ denotes Green's function from transmitter position \mathbf{r}_T to imaging point \mathbf{r} , and $G_R(\omega, \mathbf{r}, \mathbf{r}_R)$ is Green's function from imaging point \mathbf{r} to receiver position \mathbf{r}_R . Assuming a homogeneous background (air) in this scenario, these Green's functions are simply defined as:

$$G_T(\omega; \mathbf{r}_T, \mathbf{r}) \approx \exp\left(j\frac{\omega}{c_B} \|\mathbf{r} - \mathbf{r}_T\|\right) \quad (5)$$

$$G_R(\omega; \mathbf{r}, \mathbf{r}_R) \approx \exp\left(j\frac{\omega}{c_B} \|\mathbf{r}_R - \mathbf{r}\|\right) \quad (6)$$

where c_B denotes the propagation speed in the air. $w(\mathbf{r}_T, \mathbf{r}_R)$ denotes the weight term as:

$$w(\mathbf{r}_T, \mathbf{r}_R) = \exp\left\{-\frac{\|\mathbf{L}(\mathbf{r}_T, \mathbf{r}_R) - \mathbf{L}_C\|^2}{2\sigma_{\text{array}}^2}\right\} \quad (7)$$

where \mathbf{L}_C and $\mathbf{L}(\mathbf{r}_T, \mathbf{r}_R)$ denote the equivalent array locations for the center and the combination of $\mathbf{r}_T, \mathbf{r}_R$. This weight term could suppress the side-lobe effect in reconstruction images, while the azimuth resolution is slightly degraded, and σ_{array} is set to the order of array aperture length. Note that Eq. (4) is equivalent to the delay and sum (DAS) or back projection algorithm. Figure 2 shows the conceptual diagram and actual processing flow of the proposed method.

3. Results

3.1 Experimental Setting

This section describes the experimental tests with 79 GHz band FMCW MIMO radar with 4.0 GHz bandwidth (range

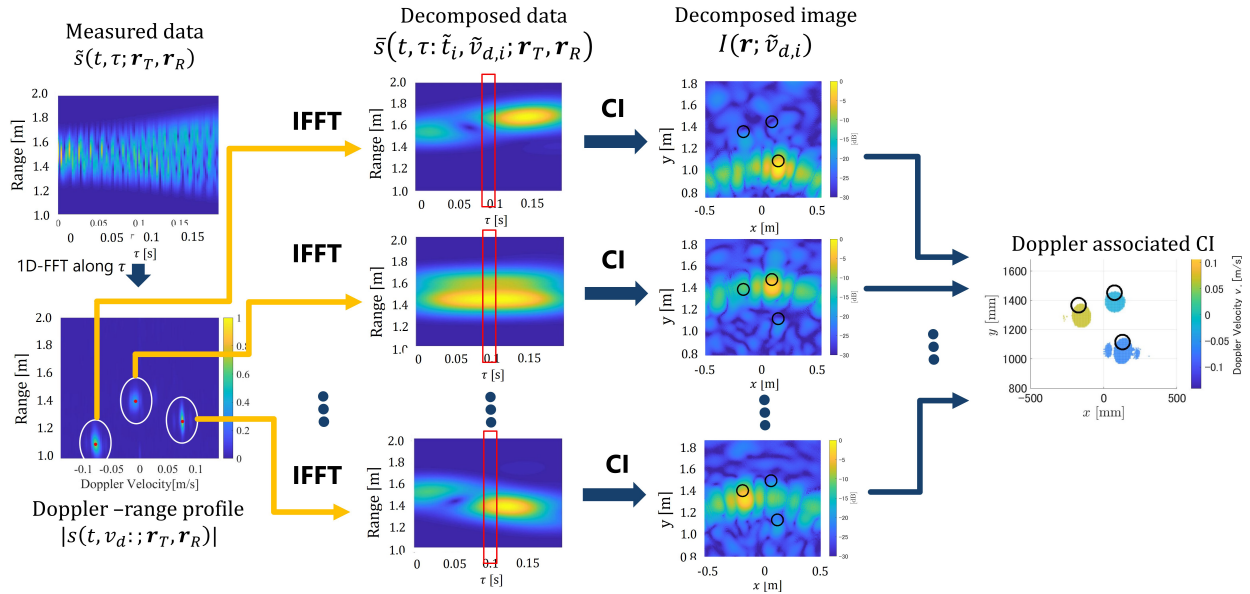


Fig. 2 Schematic diagram of the proposed method. Black circles in CI images denote the actual target shapes and locations. Red dots in the Doppler-range profiles denote the extracted local maxima.

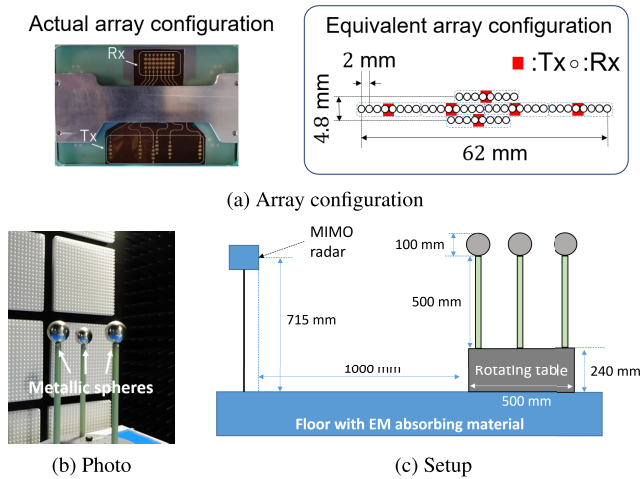


Fig. 3 79 GHz MMW MIMO radar and experimental setup.

Table 1 Parameters for 79 GHz band FMCW MIMO radar.

Center frequency	79.0 GHz
Band width	4.0 GHz
Horizontal beamwidth	45 degrees
Vertical beamwidth	10 degrees
Output power	10 dBm
Transmitters × Receivers	6 × 8
Azimuth angular resolution	1.82 degrees
Elevation angular resolution	44.68 degrees
PRI	7.0 ms
Unambiguous velocity range	± 0.141 m/s

resolution of 37.5 mm), which is a product of Sakura Tech Corp, shown in Fig. 3. Note that the 79 GHz MMW band is one of the most prevalent bands and is often used in automotive radar or other sensing applications. The six transmitters

and 8 receivers with patch antennas (10 dBm output power) configure a 6 × 8 MIMO array located on $(x, y, z) = (0, 0, 0)$, where the actual and virtual array configuration are shown in Fig. 3(a). The vertical distance from the floor to the center of array is 715 mm. The horizontal and vertical dimensions are denoted as 62 mm and 4.8 mm, respectively, and the azimuth and elevation angular resolutions are 1.82 and 44.68 degrees, respectively. Since the vertical and horizontal 3 dB beamwidths of the patch antenna are 10 and 45 degrees, respectively, we should assess the cross-sectional image at a radar height of approximately $-100 \text{ mm} \leq z \leq 100 \text{ mm}$. A quasi 2-D imaging model is assumed here. The PRI, i.e., the sampling interval of τ , is 7 ms, and thus, the unambiguous velocity range is estimated as $\pm 0.141 \text{ m/s}$. The number of all pulse hits is 380, and the total observation time is 2.66 s. Here, the CPI, i.e., the temporal resolution is set to 0.133 s (19 pulse hits), leading to $1.39 \times 10^{-2} \text{ m/s}$ velocity resolution.

3.2 Case for Rotating Three Metallic Spheres

We investigated a case involving three rotating metallic spheres, each with a diameter of 100 mm, positioned at a central height of 790 mm (closely matching the radar height of 715 mm) as illustrated in Fig. 3(b) and (c). This setup allowed us to conduct a reliable error analysis for both the Doppler velocity and the location of targets at each slow time. A stop and go observation model is used to provide an accurate ground truth profile of velocity and location. The rotation velocity is set to $2\pi/15 \text{ rad/s}$. The distance from the transmitter and receiver to the rotation axis is set to 1250 mm, and the distance from each target to the rotation center is 217 mm. First, Fig. 4(a) shows the range-Doppler velocity space profile at the specific slow time at $\tau = 1.12 \text{ s}$,

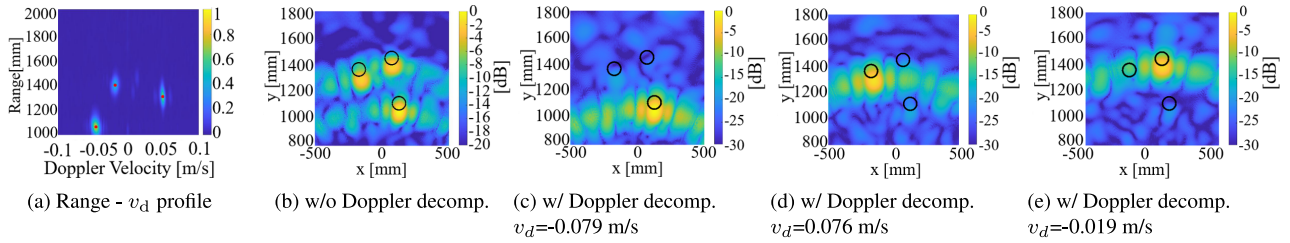


Fig. 4 Reconstruction results at the specific slow time $\tau = 1.12$ s. Black circles denote the actual target shapes and locations. Black circles from (b) to (e) denote the actual target shapes and locations. Red dots in (a) denote extracted local maxima.

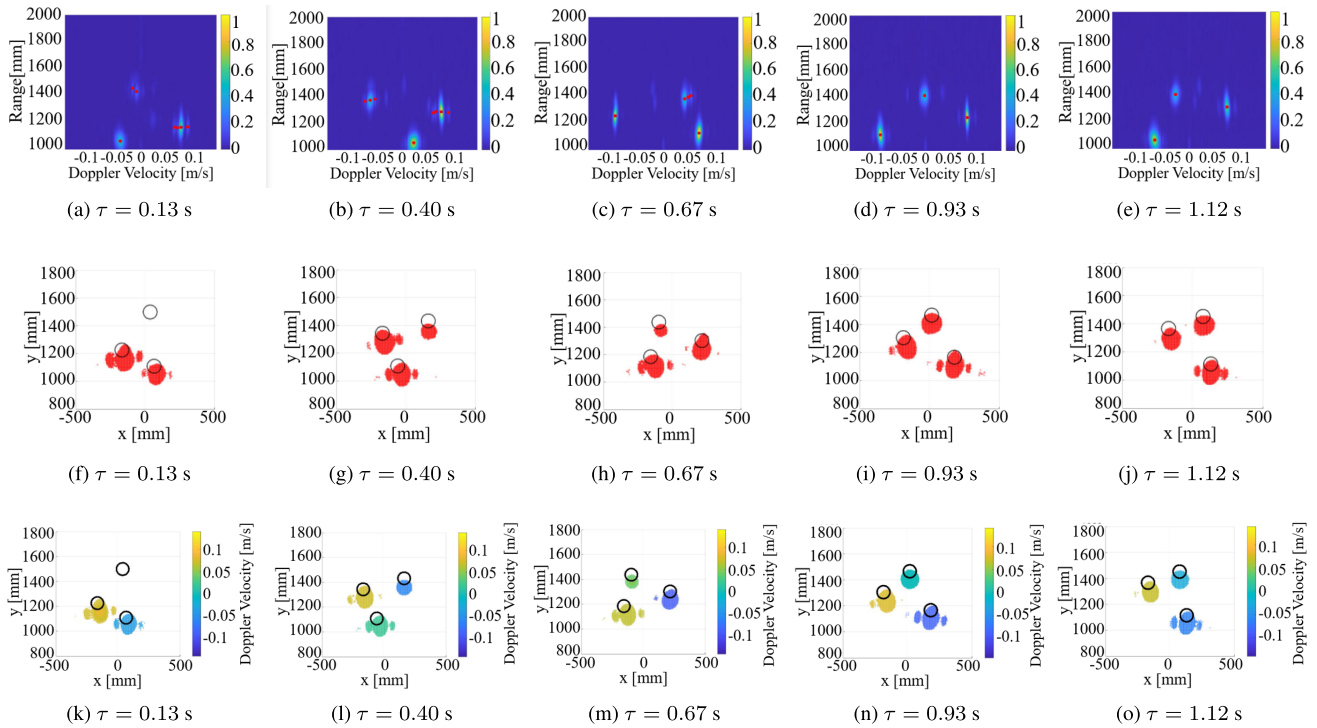


Fig. 5 Results at each slow time. Color denotes the Doppler velocity. 1st line: Range- v_d profiles. 2nd line: Reconstructions w/o Doppler velocity decomposition. 3rd line: Reconstructions w/ Doppler velocity decomposition (the proposed method). Black circles from (f) to (o) denote the actual target shapes and locations. Red dots in (a), (b), (c), (d), and (e) denote extracted local maxima.

and reveals that each Doppler response is clearly separated due to high Doppler velocity resolution. Parameter α was set to 0.1 in Eq. (2), a value chosen to balance the main and side-lobe ratios in the range- v_d space and to minimize false detection due to sidelobe responses. Also, Fig. 4(b)–(e) compares the reconstruction results without and with Doppler velocity decomposition, where the acronyms of “w/” and “w/o” denote “with” and “without”, respectively. Here, the window size used in Eq. (3), is set to 50 mm/s. These results demonstrate that our proposed scheme (w/ Doppler velocity decomp.) successfully separates each spherical target, while the conventional scheme (w/o Doppler decomp.) suffers from interfered responses, especially for far-side two objects, due to insufficient azimuth resolution or side-lobe effects. It is important to note that all reconstructed images are focused on the boundary points of the spherical targets,

rather than their centers, because the reflection points (scattering centers) are located on the metallic boundaries of the spheres owing to surface reflection.

To demonstrate the advantage of the proposed method, namely, Doppler associated imaging, Fig. 5 shows the results at other slow time, where the radar images were binarized by using the threshold (0.2 times greater than maximum response) and be associated by the Doppler velocity with color in the proposed method. Here, the weighting parameter in Eq. (7), i.e., σ_{array} is set at 15 mm in the proposed method and is one-quarter of the array aperture. These figures show that while the traditional image (w/o Doppler decomp.) suffers from interfered responses among multiple objects, the proposed approach with Doppler decomposition provides a more accurate radar image for each target. Notably, the proposed scheme does not require the Doppler

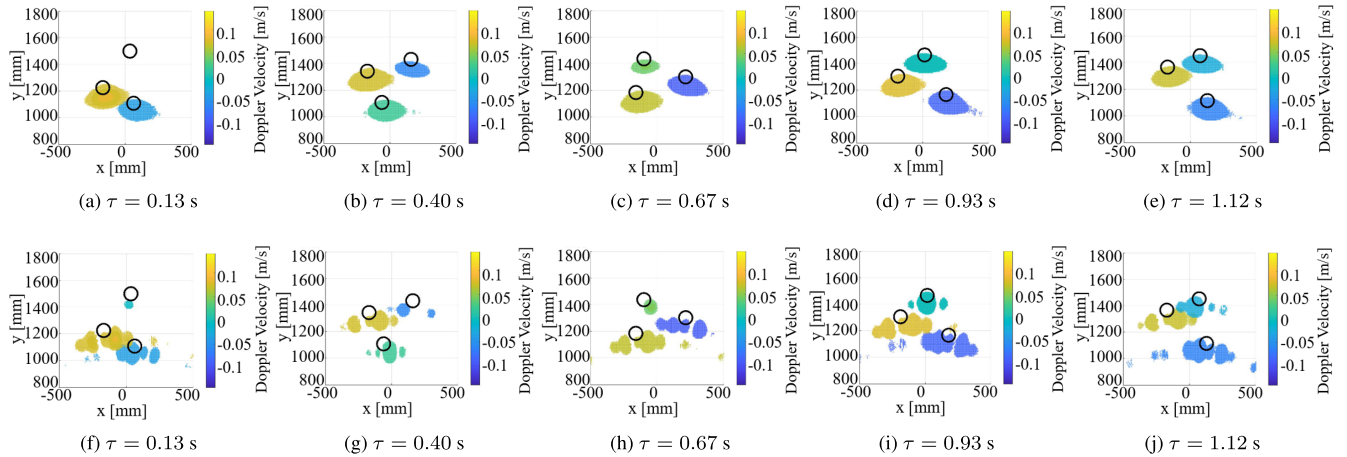


Fig. 6 Reconstruction results by the proposed method using different parameters of σ_{array} in Eq. (7). Black circles denote the actual target shapes and locations. 1st row: $\sigma_{\text{array}} = 7.5$ mm. 2nd row: $\sigma_{\text{array}} = 31$ mm.

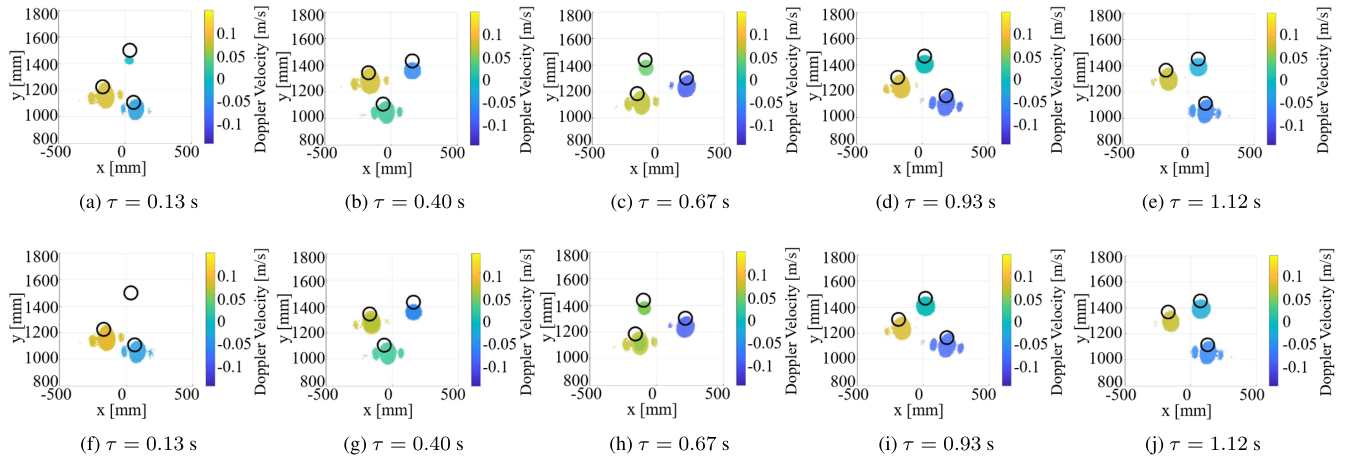


Fig. 7 Reconstruction results using different parameters of W_{v_d} used in Eq. (3). Black circles denote the actual target shapes and locations. 1st row: $W_{v_d} = 25$ mm/s. 2nd row: $W_{v_d} = 100$ mm/s.

frequency compensation, like range-Doppler algorithm in ISAR process, because it clusters the data in terms of different Doppler velocities and provides separated CI images associated with each Doppler velocity.

Herein, we investigate the sensitivity to σ_{array} in Eq. (7) in the proposed method. Figure 6 shows the reconstruction results using the proposed method when the parameter σ_{array} is changed as $\sigma_{\text{array}} = 7.5$ mm and $\sigma_{\text{array}} = 31$ mm, where $\sigma_{\text{array}} = 15$ mm is set in previous results in Fig. 5. As shown in Fig. 6, the parameter σ_{array} considerably affects the reconstruction results. For example, if σ_{array} is smaller than an equivalent array aperture length, it can suppress the side-lobe effect, incurring a lower angular resolution. If the σ_{array} is larger, then, an inverse effect would occur. Thus, the σ_{array} is set to 15 mm, so that it can balance the side-lobe suppression and angular resolution.

Moreover, Fig. 7 shows the reconstruction results, where the window length (W_{v_d}) used in Eq. (3) is changed to evaluate a sensitivity to this parameter, where $W_{v_d} = 50$ mm

is set in the previous results in Fig. 5. These figures demonstrate that the parameter W_{v_d} does not significantly affect each Doppler decomposed image, because the spatial resolution of radar image is affected by the aperture length, and is not directly related to W_{v_d} . As denoted in Sect. 2, the window length (W_{v_d}) should be determined by the Doppler velocity resolution (given by the assumed CPI and wavelength), because each reflection response with same Doppler velocity is distributed in v_d space within the Doppler velocity resolution. Setting this parameter smaller than the velocity resolution would result in data loss and a decrease in the signal-to-noise ratio (SNR), because each target's response in the Doppler velocity space would be spread over an area greater than the Doppler velocity resolution. In cases of low SNR, when the response in Doppler velocity space is obscured by noise, the proposed CI scheme risks generating false images in the reconstructed image. On the contrary, the larger value incurs an interference from different velocity components, which degrades the separation performance. If the object

has a motion with high acceleration, namely, the Doppler velocity could not be static in the assumed CPI, the Doppler response would be dispersed in v_d space, and we need to take a larger window length to avoid the loss of the reflection data from each object. Nonetheless, from the above discussion, the appropriate parameter of W_{v_d} should be set in considering the Doppler resolution. Notably, the CPI used in the proposed method should be also determined by considering the balance between the temporal and Doppler velocity resolutions. This is because the change in Doppler velocity in CPI (temporal resolution) facilitates the spread of the response along the v_d direction. An appropriate CPI can be determined based on whether a desired velocity resolution is available in the range and Doppler velocity profile.

The computational complexity of the proposed scheme was assessed by comparing the actual computational times of the conventional and the proposed CI schemes, which were approximately, 60 s and 300 s, respectively, to obtain each reconstruction image in the single CPI, using Inter(R) Xeon(R) Gold 5218 CPU @ 2.30 GHz (four processors) with 3.7 TB RAM. This is because the proposed method involves numerous CI reconstructions corresponding to the number of clusters (two or three in this case) identified in the Doppler velocity space, where the STFT process along τ in each cell of the fast time t is also required. Consequently, the proposed scheme requires significantly more computational time than the conventional method. However, since CI reconstructions in the proposed method can be processed in parallel, leveraging a GPU processor for parallel computation appears promising for addressing these challenges.

3.3 Case for Real Walking Human

Next, the case for a real human walking model was investigated. The experimental setup included a subject with a height of 178 cm, positioned 1.5 m from the radar, performing a stepping motion with an average period of 1.3 s, as depicted in Fig. 8(b). To assess the reconstruction results with quantitative criteria, the simple referential model is introduced, where 11 ellipsoids express each arm, leg, torso, and head. In addition, each part of the ellipse has a rotation and translation motion, which are determined by the actual motion of the human within the video. The above numerical calculation enables us to provide a referential target shape and location with different motion vectors at each slow time. Figure 8 shows the experimental setup, including the real human body, and the referential human walking snapshots using the 11 ellipsoid-based numerical model, which provides the ground truth profile for range, Doppler velocity and target location and shape using geometric optics approximation [19]. Figure 9 shows the reconstruction and post-threshold images using the CI without and with Doppler decomposition. $\alpha = 0.1$ in Eq. (2) is set in the proposed method. In this figure, there are some interfered responses between the arms, legs or torso in the original CI images. Focusing on the range-Doppler profile, there are many responses at the target (mainly torso)-existing range

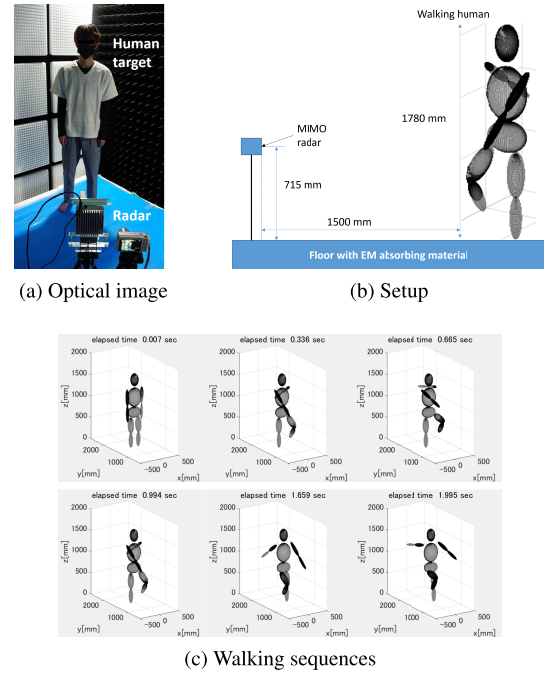


Fig. 8 Walking human in the experiment and referential human walking model at each slow time snapshot.

at 1550 mm, which are caused by multiple motions of each part, particularly at the radar height (715 mm from floor), namely, torso, left and right lower arms or upper legs. In addition, focusing on the reconstructed images, the proposed method provides the decomposed or quantitatively associated images with Doppler velocity, which would be hardly achieved by the original CI scheme without Doppler velocity decomposition.

Herein, we introduce the following error metric for threshold images in Figs. 9 as:

$$\text{Err}_{bi} = N_{\text{out}}/N_{\text{total}} \quad (8)$$

where N_{total} denotes the total number of reconstructed cells and N_{out} denotes the number of cells, that are outside from all the objects (illustrated as black ellipses in Fig. 9). Figure 10 shows Err_{bi} for each slow time, and demonstrates that our proposed method retains a certain level superiority from the original CI based method. The above differences are not significantly distinct, however, the proposed method offers more informative image associated by the Doppler velocity. Note that, since the unambiguous velocity range (± 0.141 m/s) is not enough to cover the actual velocity of each part's motion (more than 1.0 m/s), the range-Doppler profile must include aliasing responses. However, this study focuses on the Doppler based separation in the CI approach, and these aliasing effects would not be seriously affected, as long as each response could be separated. In order to associate with more accurate Doppler velocity, some incoherent scheme, such as in [17] should be introduced. It is notable that while the temporal resolution is within 0.14 s, the Doppler velocity resolution is 1.39×10^{-2} m/s, which is sufficient to resolve the multiple responses from each part, that

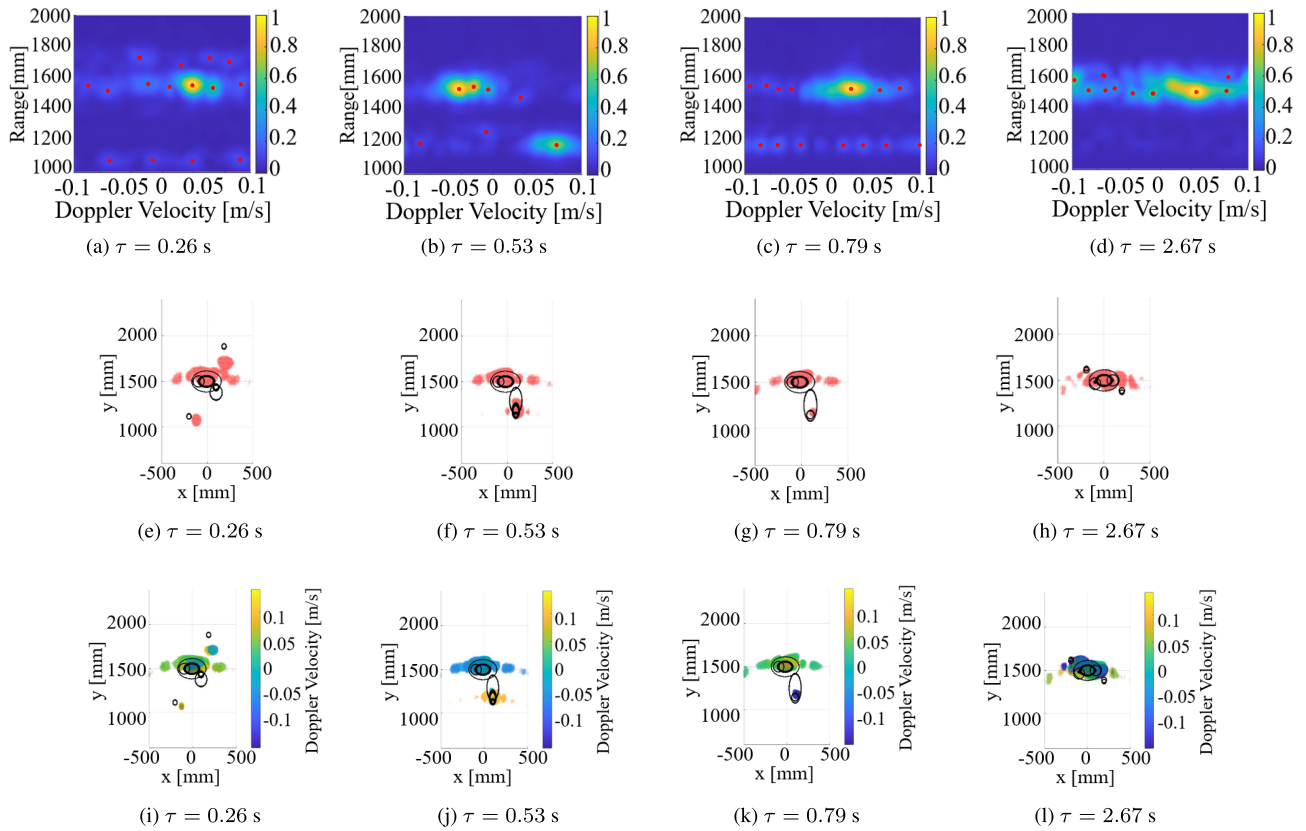


Fig. 9 Results obtained by each method at different slow times. Red dots in (a), (b), (c), and (d) denote the extracted local maxima. Black ellipsoids in the image denotes the actual cross-sectional images at $z = -100, 0$, and 100 mm. Color in (i), (j), (k), and (l) denote the Doppler velocity. 1st column: Range- v_d profile. 2nd column: Reconstruction by the original CI. 3rd column: Reconstruction by the proposed CI.

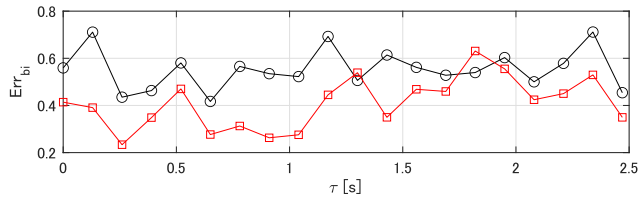


Fig. 10 Quantitative error analysis for each image as Err_{bi} . Black hollow circles denote the original CI. Red hollow squares are the proposed method.

is, the proposed scheme could exploit the advantage of the 79 GHz MMW band radar system. Notably, the proposed method requires an additional computational time as the number of extracted Doppler-range points increases. However, these processes could be computed in parallel, which would alleviate the required computation time.

4. Conclusion

This study presented the 79 GHz band MMW MIMO radar-based Doppler velocity decomposition and associated radar imaging method, where the advantages of higher Doppler velocity and temporal resolutions are well exploited. Assuming targets with multiple parts of different velocity vec-

tors, such as human walking motion, the proposed scheme introduces Doppler velocity decomposed CI processing to reconstruct the Doppler separated or associated radar image. The two experimental studies, assuming three rotating metallic spheres and a real human stepping motion model, demonstrated that our proposed scheme accurately provides a multidimensional radar image, namely, a Doppler-associated image within 0.133 s temporal resolution. These results were also compared with those of conventional CI schemes that do not utilize Doppler velocity space decomposition. The proposed method offers a significant advantage by enabling the decomposition of multiple reflection responses in the Doppler velocity space, particularly when these responses are caused by objects moving at different velocities. A quantitative error comparison further demonstrated the superiority of the proposed method for reducing false images. These features would be promising for the post-recognition process of object identification, which would be necessary for collision avoidance systems for vehicle mounted sensing applications. Nevertheless, higher frequency band extension is associated with several challenges. One such challenge is the phase synchronization issue along multiple transmitters and receivers in the MIMO radar system because the phase rotation speed becomes much higher

in the high frequency band. In addition, the array configuration in the higher frequency band is densely spaced within a half of the wavelength to suppress the ambiguous response (grating lobe). These difficulties might be alleviated by introducing a phase calibration process or a postsignal processing scheme to a sparse array configuration, such as sparse regularization. Although the experimental tests conducted in this study did not conclusively determine whether the proposed scheme could overcome the challenge of insufficient spatial resolution in far-range scenarios (beyond 10 m), there is potential for enhancing the spatial resolution by decomposing different Doppler components, which are included in the traditional angular resolution. Investigating performance in far-range situations remains an important aspect of our future work.

References

- [1] T. Kato, H. Yamada, H. Mori, "Experimental study on 3D imaging using millimeter-wave non-uniform 2D-MIMO radar," *IEICE Commun. Express*, vol.11, no.12, pp.760–765, 2022.
- [2] F. Soldovieri, A. Brancaccio, G. Prisco, G. Leone, and R. Pieri, "A Kirchhoff-based shape reconstruction algorithm for the multimono-static configuration: The realistic case of buried pipes," *IEEE Trans. Geosci. Remote Sens.*, vol.46, no.10, pp.3031–3038, Oct. 2008.
- [3] J.M. Lopez-Sanchez and J. Fortuny-Guasch, "3-D radar imaging using range migration techniques," *IEEE Trans. Antennas Propag.*, vol.48, no.5, pp.728–737, May 2000.
- [4] X. Zhuge and A.G. Yarovoy, "Three-dimensional near-field MIMO array imaging using range migration techniques," *IEEE Trans. Image Process.*, vol.21, no.6, pp.3026–3033, June 2012.
- [5] Z. Wang, Q. Guo, X. Tian, T. Chang, and H.L. Cui, "Near-field 3-D millimeter-wave imaging using MIMO RMA with range compensation," *IEEE Trans. Microwave Theory Techn.*, vol.67, no.3, pp.1157–1166, March 2019.
- [6] R. Zhu, J. Zhou, G. Jiang, and Q. Fu, "Range migration algorithm for near-field MIMO-SAR imaging," *IEEE Geosci. Remote Sens. Lett.*, vol.14, no.12, pp.2280–2284, Dec. 2017.
- [7] A. Salehi-Barzegar, A. Cheldavi, V. Nayyeri, and A. Abdolali, "A Fast diffraction tomography algorithm for 3-D through-the-wall radar imaging using nonuniform fast Fourier transform," *IEEE Geosci. Remote Sens. Lett.*, vol.19, pp.1–5, 2022.
- [8] S. Sadeghi, K. Mohammadpour-Aghdam, R. Faraji-Dana, and R.J. Burkholder, "A DORT-uniform diffraction tomography algorithm for through-the-wall imaging," *IEEE Trans. Antennas Propag.*, vol.68, no.4, pp.3176–3183, April 2020.
- [9] J. Yang, T. Jin, and X. Huang, "Compressed sensing radar imaging with magnitude sparse representation," *IEEE Access*, vol.7, pp.29722–29733, 2019.
- [10] M. Miller, J. Hinz, M. Saquib, and A.J. Blanchard, "Adjustable transmitter spacing for MIMO radar imaging with compressed sensing," *IEEE Sensors J.*, vol.15, no.11, pp.6671–6677, Nov. 2015.
- [11] F. Gu, Q. Zhang, L. Chi, Y. Chen, and S. Li, "A novel motion compensating method for MIMO-SAR imaging based on compressed sensing," *IEEE Sensors J.*, vol.15, no.4, pp.2157–2165, April 2015.
- [12] S. Xu and A. Yarovoy, "Motion-based separation and imaging of closely spaced extended targets," *IEEE Sensors J.*, vol.20, no.22, pp.13542–13551, Nov. 2020.
- [13] T. Ohmori and S. Kidera, "Doppler velocity enhanced range migration algorithm for high resolution and noise-robust three-dimensional radar imaging," *IEEE Sensors J.*, vol.21, no.18, pp.20616–20628, Sept. 2021.
- [14] Z. Xu, C.J. Baker, and S. Pooni, "Range and Doppler cell migration in wideband automotive radar," *IEEE Trans. Veh. Technol.*, vol.68, no.6, pp.5527–5536, June 2019.
- [15] J.M. Munoz-Ferreras and F. Perez-Martinez, "On the Doppler spreading effect for the range-instantaneous-Doppler technique in inverse synthetic aperture radar imagery," *IEEE Geosci. Remote Sens. Lett.*, vol.7, no.1, pp.180–184, Jan. 2010.
- [16] D. Cheng, S. Pei, H. Qu, C. Chen, and W. Chen, "Removing micro-Doppler effect in ISAR imaging by promoting joint sparsity in range profile sequences and the time-frequency domain," *IEEE Sensors J.*, vol.21, no.21, pp.24613–24630, Nov. 2021.
- [17] T. Ando and S. Kidera, "k- and Doppler velocity decomposition-based range points' migration for 3-D localization with millimeter wave radar," *IEEE Sensors J.*, vol.22, no.23, pp.22850–22864, Dec. 2022.
- [18] Y. Sekigawa and S. Kidera, "Doppler velocity decomposed radar imaging method for 79 GHz band millimeter wave radar," 2022 International Symposium on Antennas and Propagation (ISAP), Sydney, Australia, pp.3–4, 2022.
- [19] V.U. Zavorotny and A.G. Voronovich, "Comparison of geometric optics and diffraction effects in radar scattering from steep and breaking waves," *Proc. IEEE International Geoscience and Remote Sensing Symposium, IGARSS 2007*, July, 2007.



Yoshiaki Sekigawa received the B.E. degree in communication engineering and informatics from the University of Electro-Communications, Tokyo, Japan, in 2022. He is currently pursuing the M.E. degree with the Graduate School of Informatics and Engineering in the University of Electro-Communications, Tokyo, Japan. His research interest includes signal processing and imaging for millimeter wave radar as well as its applications.



Shouhei Kidera received his B.E. degree in Electrical and Electronic Engineering from Kyoto University in 2003 and M.I. and Ph.D. degrees in Informatics from Kyoto University, Kyoto, Japan, in 2005 and 2007, respectively. In 2009, he joined as an Assistant Professor with the University of Electro-Communications, Tokyo, Japan, where he is currently a full Professor with Graduate School of Informatics and Engineering in the University of Electro-Communications, Tokyo, Japan.

His current research interest is in advanced radar signal processing or electromagnetic inverse scattering issue for ultra wideband (UWB) three-dimensional sensor or bio-medical applications. He has been stayed at the Cross-Disciplinary Electromagnetics Laboratory in the University of Wisconsin Madison as the visiting researcher in 2016. He has been a Principal Investigator of the PRESTO Program of Japan Science and Technology Agency (JST) from 2017 to 2021. He was a recipient of the 2012 Ando Incentive Prize for the Study of Electronics, 2013 Young Scientist's Prize by the Japanese Minister of Education, Culture, Sports, Science and Technology (MEXT), and 2014 Funai Achievement Award, 2022 KDDI Foundation Award, Contribution Award, and 2023 RIEC Award. He is a senior member of the Institute of Electrical and Electronics Engineering (IEEE), and a member of the Institute of Electrical Engineering of Japan (IEEJ), and the Japan Society of Applied Physics (JSAP).